# Coded-mask-based wavefront sensing technique for APS nanofocusing beamline diagnostics

**Xianbo Shi,**[a) ] **Zhi Qiao,** **Matthew J. Highland,** **Matthew G. Frith,** **Luca Rebuffi,**
**Michael J. Wojcik,** **and Lahsen Assoufid**

**AFFILIATIONS**

Argonne National Laboratory, 9700 S Cass Ave., Lemont, Illinois 60439, USA

[a)] **Author to whom correspondence should be addressed:** xshi@anl.gov

## ABSTRACT

We extend our recently developed coded-mask wavefront sensing technique to enable single-shot measurements of nanofocused x-ray beams. This method accurately reconstructs the focal beam profile by backpropagating the wavefront measured downstream of the beam focus. To validate its performance, we benchmarked it against the conventional fluorescence wire scan method, successfully measuring ~120 nm focal spots at the 28-ID-B beamline of the Advanced Photon Source using a polymeric compound refractive lens. The results highlight the effectiveness of coded-mask wavefront sensing for high-precision beam profiling and its application as a real-time wavefront monitoring tool.

## I. INTRODUCTION

Quantitative characterization of x-ray beam wavefronts is essential for optimizing optics alignment and guiding experiments at synchrotron light sources, particularly diffraction-limited storage rings[1] and free electron lasers. Achieving real-time, accurate measurements of nanofocused beams remains a challenge, particularly for single-shot wavefront diagnostics crucial for optical alignment and control.

Traditional methods, such as 1D edge or wire scans and direct beam imaging, have limitations in spatial resolution and require invasive setups. Ptychography[2] offers high-precision beam profiling but is experiment-specific and unsuitable for routine diagnostics. Other full-field wavefront sensing techniques, like Hartmann sensors[3] and speckle-tracking,[4,5] show promise but are limited by spatial resolution, coherence requirements, or the need for reference patterns.

To address these issues, we developed a coded-mask wavefront sensing method[6–9] that combines the strengths of grating and speckle-tracking techniques. By using a known coded mask to generate high-contrast speckle patterns, this method enables true single-shot measurements with high spatial resolution and phase sensitivity. It has also been successfully applied in adaptive optics control systems.[10]

In this study, we extend this technique to measure nanofocused x-ray beams, validating it against conventional fluorescence wire scans. We demonstrate its efficacy by profiling 120 nm focal spots at the APS 28-ID-B beamline using a polymeric compound refractive lens (CRL), showcasing its application as a real-time wavefront monitoring tool.

## II. METHODOLOGY

### A. Coded-mask wavefront sensing

A coded mask is a synthetic modulator that generates high-contrast patterns when placed in an x-ray beam. By comparing these patterns with simulations from an ideal wavefront (e.g., plane or spherical), the phase information of the beam can be extracted. The measurement requires only a single 2D intensity distribution $I_{\text{exp}}(\mathbf{r})$ captured on the transverse plane $(x, y)$ with a scintillator-based detector. A schematic of the measurement geometry for a focused beam is illustrated in Fig. 1. The workflow for data analysis is detailed below:

(I) *Image Loading and Preprocessing*. The raw image is normalized by subtracting the dark image $I_{\text{dark}}(\mathbf{r})$ and, if available, normalizing by the flat field image $I_{\text{flat}}(\mathbf{r})$ (taken without the mask in the beam path).

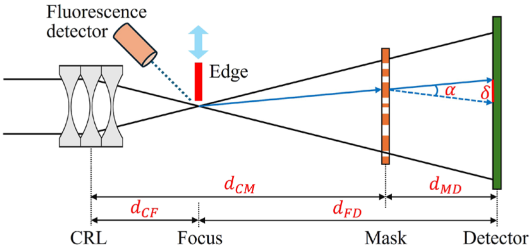

**FIG. 1.** Schematic of the coded-mask wavefront sensing geometry for a focused beam. The distances are defined as follows: $d_{CF}$–CRL to focus, $d_{CM}$–CRL to mask, $d_{MD}$–mask to detector, and $d_{FD}$–focus to detector.

(II) *Pattern Generation and Propagation*. The coded mask's known design is used to simulate an image, $I_{\text{sim}}(\mathbf{r})$, at the detector plane, assuming an ideal wavefront. Typically, a toroidal wavefront is used, with its radii of curvature defined as the estimated focus-to-detector distances along the $x$ and $y$ axes. The beam's partial coherence is modeled by convolving the simulated image with a blur representing the estimated focal spot size.

(III) *Pattern Alignment*. A search algorithm aligns the simulated pattern $I_{\text{sim}}(\mathbf{r})$ with the experimental image $I_{\text{exp}}(\mathbf{r})$ to determine displacements across the image for optimal pattern matching.

(IV) *Focus-to-Detector Distance Recalculation (Optional)*. If necessary, an additional adjustment to the estimated focus-to-detector distance, $d_{FD}$, is performed based on the scaling factor derived from the pattern size in the experimental and simulated images. This requires repeating steps (II) and (III) once more using the updated distance estimate.

(V) *Speckle Tracking*. This core analytical process involves tracking the speckle pattern to obtain the 2D pixel displacement field $\delta(\mathbf{r})$ across the detector plane using the wavelet-transform-based x-ray speckle tracking (WXST) method.[7,8]

(VI) *Wavefront Reconstruction*. The displacement fields $\delta(\mathbf{r})$ are used to compute local beam deflection angles $\alpha(\mathbf{r}) = \delta(\mathbf{r})/d_{MD}$, as viewed from the mask plane, where $d_{MD}$ is the mask-to-detector distance. The phase gradient at the detector plane is then given by

$$\nabla\phi(\mathbf{r}) = \left(\frac{2\pi}{\lambda}\right)\alpha(\mathbf{r})f_p = \frac{2\pi\delta(d_{FD}-d_{MD})}{\lambda d_{MD}d_{FD}}, \tag{1}$$

where $\lambda$ is the x-ray wavelength, and the projection factor $f_p = (d_{FD}-d_{MD})/d_{FD}$ accounts for the magnification of the deflection angle from the mask plane to the detector plane. The wavefront phase $\phi(\mathbf{r})$ is reconstructed by 2D integration of $\nabla\phi(\mathbf{r})$, using techniques like the Frankot–Chellappa algorithm.[11] The wavefront amplitude, $A(\mathbf{r})$, is obtained as the magnitude of the flat field image, $\sqrt{I_{\text{flat}}(\mathbf{r})}$, or, when $I_{\text{flat}}(\mathbf{r})$ is not available, from the filtered speckle image, $\sqrt{I_{\text{exp}}(\mathbf{r})}$.

## B. Wavefront backpropagation

Following step (VI) mentioned earlier, both the amplitude and phase of the wavefront at the detector plane are retrieved and combined to form the wavefront field,

$$U(\mathbf{r}) = A(\mathbf{r})\exp\left[i\phi(\mathbf{r})\right]. \tag{2}$$

To locate the beam waist, $U(\mathbf{r})$ is propagated in free space to a distance where the beam size is minimized. The angular-spectrum form of the Fresnel diffraction integral is used, incorporating a user-defined grid scaling factor $s$, which adjusts the real-space sampling interval to accommodate the changing beam size during propagation.

Referring to Eq. (6.65) in Ref. [12], the wavefront propagation over a distance $\Delta d$ from the $\mathbf{r}_1$ plane to the $\mathbf{r}_2$ plane is described as

$$U(\mathbf{r}_2) = \mathcal{Q}\left[\frac{s-1}{s\Delta d},\mathbf{r}_2\right]\mathcal{F}^{-1}\left[\mathbf{f}_1,\frac{\mathbf{r}_2}{s}\right] \times \mathcal{Q}\left[-\frac{4\pi^2\Delta d}{ks},\mathbf{f}_1\right]\mathcal{F}[\mathbf{r}_1,\mathbf{f}_1] \times \mathcal{Q}\left[\frac{1-s}{\Delta d},\mathbf{r}_1\right]\left\{\frac{U(\mathbf{r}_1)}{s}\right\}, \tag{3}$$

where $k = 2\pi/\lambda$ is the wavenumber and $\mathbf{f}_1$ and $\mathbf{f}_2$ are spatial frequencies. The operators are

$$\mathcal{Q}[b,\mathbf{r}]\{U(\mathbf{r})\} \equiv e^{i\frac{k}{2}b|\mathbf{r}|^2}U(\mathbf{r}), \tag{4}$$

$$\mathcal{F}[\mathbf{r},\mathbf{f}]\{U(\mathbf{r})\} \equiv \int_{-\infty}^{\infty} U(\mathbf{r})e^{-i2\pi\mathbf{f}\cdot\mathbf{r}}d\mathbf{r}, \tag{5}$$

$$\mathcal{F}^{-1}[\mathbf{f},\mathbf{r}]\{U(\mathbf{f})\} \equiv \int_{-\infty}^{\infty} U(\mathbf{f})e^{i2\pi\mathbf{f}\cdot\mathbf{r}}d\mathbf{f}. \tag{6}$$

The scaling factor $s$ is adjusted empirically to balance spatial resolution and field of view, being fine enough to resolve the focal spot and broad enough to capture the full extent of the beam. In this study, the Python package *wofry*[13] is utilized to perform the propagation, allowing for different scaling factors $s_x$ and $s_y$ for the two orthogonal directions.

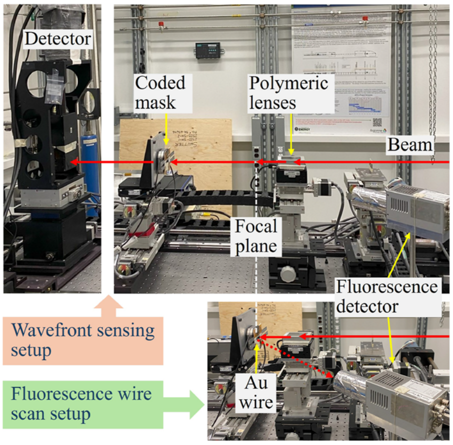

**FIG. 2.** Experimental configuration at the APS 28-ID-B IDEA beamline showing both the wavefront sensing setup (top) and the fluorescence wire scan setup (bottom).

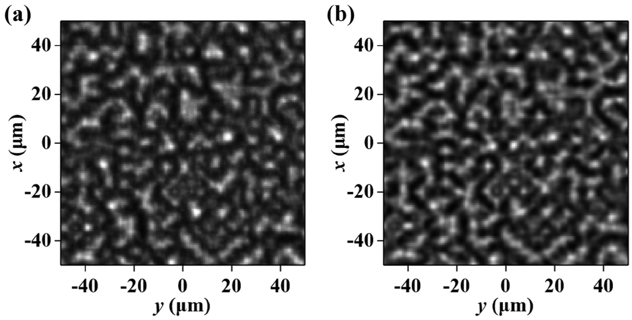

FIG. 3. (a) Raw image of the beam modulated by the coded mask. (b) Simulated image generated after the workflow step (IV) in Sec. II A.

## III. EXPERIMENTS

The experiment was conducted at the 28-ID-B Instrumentation Development, Evaluation & Analysis Beamline (IDEA) beamline of APS, with a photo of the experimental setup shown in Fig. 2. The beamline had two horizontally oriented mirrors and a double-multilayer monochromator to tune the x-ray energy to 20 keV with an energy bandwidth of 1%. A polymeric CRL,[14] positioned 67 m from the source, generated a 2D focused beam 120 mm downstream. The coded mask for the wavefront sensing was placed 400 mm downstream of the CRL ($d_{CM}$ = 400 mm), and the detector was 200 mm further downstream ($d_{MD}$ = 200 mm).

The coded mask was fabricated from electroplated gold (1.5 $\mu$m thick) on a 1 μm-thick silicon nitride membrane, with a total patterned area of 2 × 2 mm$^2$. The pattern consists of a random 2D array of 2 $\mu$m squares with a 50% fill factor. The fabrication process is described in detail in Ref. 15. The detector system comprised a 20 $\mu$m thick LuAG:Ce scintillator, a 10× objective lens, and a Zyla 5.5 sCMOS camera, which had an effective pixel size of 0.65 $\mu$m.

For benchmarking, a fluorescence wire scan setup was integrated as shown in Fig. 2. A 200 nm wide Au wire coated on a silicon nitride membrane was placed in the beam path, and a Vortex silicon drift detector, positioned at a 135° angle from the x-ray beam, detected the fluorescence signal. The motorized system allowed for precise scans along the $x$ and $y$ axes, with a resolution of 20 nm.

## IV. RESULTS

The accuracy of the speckle-tracking process relies heavily on the accurate simulation of the coded mask pattern on the detector. Figure 3(a) shows the raw beam image modulated by the coded mask. The corresponding simulated image after the workflow step (IV) in Sec. II A is presented in Fig. 3(b), demonstrating a strong match with the measured image. This confirms that the simulation effectively captures the main curvature and coherence of the beam. Subtle variations between the patterns contain the key information needed to reconstruct the phase gradient as per Eq. (1).

Applying the WXST analysis,[8] the displacement fields along the $x$ and $y$ directions were retrieved, as shown in Figs. 4(a) and 4(b). These fields are primarily linear, corresponding to the main curvature of the wavefront. The reconstructed wavefront phase $\phi(\mathbf{r})$ was obtained via 2D integration and shown in Fig. 4(c). Embedded within this dominant spherical curvature are finer phase errors introduced by the CRL, which ultimately influence the focus quality.

In this study, $I_{\text{flat}}(\mathbf{r})$ was not directly measured; instead, a uniform filter was applied to $I_{\text{exp}}(\mathbf{r})$ to eliminate the speckle pattern.

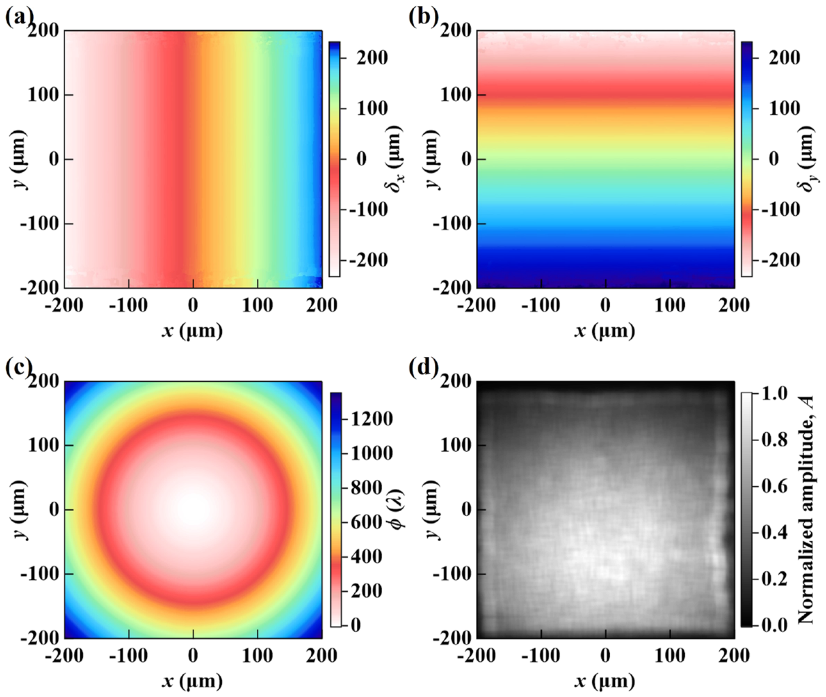

FIG. 4. Displacement fields along the $x$ direction (a) and $y$ direction (b) reconstructed using the WXST analysis. (c) Reconstructed wavefront phase after 2D integration. (d) Amplitude of the wavefront computed from the square root of the uniformly filtered $I_{\text{exp}}(\mathbf{r})$.

Each pixel value was replaced with the mean of the pixel values within a window size of ten pattern periods. Tests with filter sizes ranging from 2 to 20 periods showed minimal differences in focal spot size, confirming the robustness of this approach. The amplitude $A(\mathbf{r})$ shown in Fig. 4(d) was the square root of the uniformly filtered $I_{\text{exp}}(\mathbf{r})$.

The wavefront is constructed from the extracted amplitude and phase using Eq. (2). The backpropagation results at different longitudinal distances $z$ along the horizontal and vertical directions are shown in Figs. 5(a) and 5(c). From these, we identify the beam waist in both directions, where the beam size reaches its minimum.

It is important to note that various metrics can define beam size, such as the FWHM, the FWHM of a Gaussian fit, and the RMS size over a given range. However, since the beam profiles in this study deviate significantly from a Gaussian shape and exhibit multiple side peaks, we used the direct FWHM values. This approach emphasizes the smallest achievable beam width and provides insight into the spatial resolution of the method.

The focused beam profiles at the horizontal and vertical waists are shown in Figs. 5(b) and 5(d), respectively. For comparison, beam profiles from the fluorescence wire scan are also plotted as circle markers. The wavefront sensing results demonstrate higher spatial resolution, revealing more detailed profile features. In addition, the wire scan measurements are influenced by the wire's 200 nm width, which must be subtracted in quadrature from the measured beam size. The extracted FWHM sizes from the fluorescence wire scan are 0.11 $\mu$m in $x$ and 0.24 $\mu$m in $y$, while those from the wavefront sensing are 0.12 $\mu$m in $x$ and 0.21 $\mu$m in $y$. The agreement in both directions is within the acceptable range, considering the level of measurement precision.

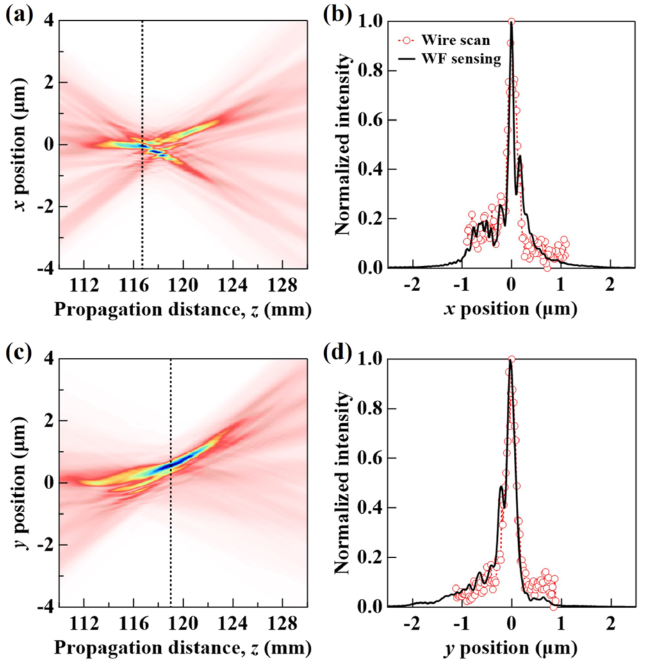

**FIG. 5.** Wavefront backpropagation results showing the beam size as a function of longitudinal distance along the (a) $x$ and (c) $y$ directions, with dotted lines indicating the beam waist, where the beam reaches its minimum size. The focused beam profiles at the (b) horizontal and (d) vertical waists from wavefront sensing (solid lines) are compared with those from the fluorescence wire scan (circular markers).

The horizontal and vertical waist positions from the wavefront sensing show a discrepancy of a few millimeters, indicating astigmatism, which does not align with the wire scan results. This suggests the presence of a second-order systematic error in the wavefront data. By removing an estimated second-order term from the wavefront phase before propagation, we achieve matching longitudinal waist positions in both directions, while the focal spot size and shape remain largely unaffected. A calibration procedure is currently under development to correct this systematic error, primarily addressing detector distortion.

## V. CONCLUSIONS

In this study, we successfully extended our coded-mask wavefront sensing technique to enable single-shot measurements of nanofocused x-ray beams. The method was validated against the conventional fluorescence wire scan at the APS 28-ID-B beamline, showing superior spatial resolution and accuracy in detecting fine beam features. We demonstrated that this technique can accurately reconstruct the focal beam profile and provide real-time wavefront monitoring with minimal deviation in focal spot size and shape.

The technique has proven effective for focal spots down to ~100 nm, with resolution primarily determined by the number of pixels the beam spans on the detector. Achieving optimal performance requires careful selection and configuration of the mask, detector, and geometry tailored to the specific focusing optics. To support this, we have developed a set of standard wavefront sensors optimized for various APS beamlines.[16] For even smaller beams, precise characterization and correction of detector distortion may become increasingly important.

These results underscore the potential of coded-mask wavefront sensing as a robust diagnostic tool for advanced synchrotron beamline operations, enabling precise beam profiling and alignment optimization.

## ACKNOWLEDGMENTS

This research used resources from the Advanced Photon Source and the Center for Nanoscale Materials, U.S. Department of Energy (DOE) Office of Science User Facilities, operated for the DOE Office of Science by Argonne National Laboratory under Contract No. DE-AC02-06CH11357. Work by Matthew J. Highland was also supported by the U.S. Department of Energy, Office of Science, Office of Basic Energy Sciences, Materials Science and Engineering Division.

## AUTHOR DECLARATIONS

### Conflict of Interest

The authors have no conflicts to disclose.

### Author Contributions

**Xianbo Shi**: Conceptualization (lead); Data curation (equal); Formal analysis (lead); Software (equal); Supervision (lead); Validation (lead); Writing – original draft (lead); Writing – review & editing (lead). **Zhi Qiao**: Conceptualization (supporting); Data curation (equal); Formal analysis (supporting); Software (equal); Writing – review & editing (supporting). **Matthew J. Highland**: Data curation (supporting); Resources (supporting); Validation (supporting); Writing – review & editing (supporting). **Matthew G. Frith**: Data curation (supporting); Resources (supporting); Validation (supporting); Writing – review & editing (supporting). **Luca Rebuffi**: Software (equal); Validation (supporting); Writing – review & editing (supporting). **Michael J. Wojcik**: Conceptualization (supporting); Resources (supporting); Validation (supporting); Writing – review & editing (supporting). **Lahsen Assoufid**: Funding acquisition (lead); Resources (supporting); Validation (supporting); Writing – review & editing (supporting).

## DATA AVAILABILITY

The data that support the findings of this study are available from the corresponding author upon reasonable request.

## REFERENCES

[1] M. Eriksson, J. F. Van Der Veen, and C. Quitmann, J. Synchrotron Radiat. **21**, 837 (2014).

[2] F. Seiboth, M. Kahnt, M. Scholz, M. Seyrich, F. Wittwer, J. Garrevoet, G. Falkenberg, A. Schropp, and C. G. Schroer, Proc. SPIE **9963**, 99630P (2016).

[3] M. Idir, P. Mercere, M. H. Modi, G. Dovillaire, X. Levecq, S. Bucourt, L. Escolano, and P. Sauvageot, Nucl. Instrum. Methods Phys. Res., Sect. A **616**, 162 (2010).

[4] S. Berujon, R. Cojocaru, P. Piault, R. Celestre, T. Roth, R. Barrett, and E. Ziegler, J. Synchrotron Radiat. **27**, 284 (2020).

[5] S. Berujon, R. Cojocaru, P. Piault, R. Celestre, T. Roth, R. Barrett, and E. Ziegler, J. Synchrotron Radiat. **27**, 293 (2020).

[6] Z. Qiao, X. Shi, M. J. Wojcik, L. Rebuffi, and L. Assoufid, Appl. Phys. Lett. **119**, 011105 (2021).

[7] Z. Qiao, X. Shi, R. Celestre, and L. Assoufid, Opt. Express **28**, 33053 (2020).

[8] Z. Qiao, X. Shi, and L. Assoufid, Proc. SPIE **11492**, 114920O (2020).

[9] Z. Qiao, X. Shi, Y. Yao, M. J. Wojcik, L. Rebuffi, M. J. Cherukara, and L. Assoufid, Optica **9**, 391 (2022).

[10] L. Rebuffi, X. Shi, Z. Qiao, M. J. Highland, M. G. Frith, A. Wojdyla, K. A. Goldberg, and L. Assoufid, Opt. Express **31**, 21264 (2023).

[11] R. T. Frankot and R. Chellappa, IEEE Trans. Pattern Anal. Mach. Intell. **10**, 439 (1988).

[12] J. D. Schmidt, *Numerical Simulation of Optical Wave Propagation with Examples in MATLAB* (SPIE, 2010).

[13] L. Rebuffi and M. Sanchez del Rio, Proc. SPIE **10388**, 1038808 (2017).

[14] Z. Qiao, X. Shi, P. Kenesei, A. Last, L. Assoufid, and Z. Islam, Rev. Sci. Instrum. **91**, 113703 (2020).

[15] S. Marathe, X. Shi, M. J. Wojcik, A. T. Macrander, and L. Assoufid, J. Visualized Exp. **116**, e53025 (2016).

[16] M. G. Frith, M. J. Highland, Z. Qiao, L. Rebuffi, L. Assoufid, and X. Shi, Rev. Sci. Instrum. **94**, 123102 (2023).